

# Long-term variation in dissolved inorganic carbon and ocean acidification indices in the Northwest Pacific from 1993 to 2018: A study of a biogeochemical model with an operational ocean model product and observational evidence

Miho Ishizu (✉ [mishizu@jamstec.go.jp](mailto:mishizu@jamstec.go.jp))

Japan Agency for Marine-Earth Science and Technology <https://orcid.org/0000-0002-3035-7655>

Yasumasa Miyazawa

Japan Marine Science and Technology Center: Kaiyo Kenkyu Kaihatsu Kiko

Xinyu Guo

Ehime University, Center for Marine Environmental Studies

---

## Research Article

**Keywords:** biogeochemical model, Northwest Pacific, ocean acidification, ocean alkalinization, JCOPE

**Posted Date:** June 7th, 2021

**DOI:** <https://doi.org/10.21203/rs.3.rs-165133/v1>

**License:**  This work is licensed under a Creative Commons Attribution 4.0 International License.

[Read Full License](#)

---

1 Long-term variation in dissolved inorganic carbon and ocean acidification  
2 indices in the Northwest Pacific from 1993 to 2018: A study of a  
3 biogeochemical model with an operational ocean model product and  
4 observational evidence

5

6 Miho Ishizu<sup>1</sup>, Yasumasa Miyazawa<sup>2</sup>, Xinyu Guo<sup>3</sup>

7

8 <sup>1</sup>E-mail: [mishizu@jamstec.go.jp](mailto:mishizu@jamstec.go.jp)

9 Japan Agency for Marine-Earth Science and Technology, Environmental Variability Prediction and  
10 Application Research Group, Yokohama Institute for Earth Sciences, 3173-25 Showa-machi,  
11 Kanagawa-ku, Yokohama 236-0001, Japan

12 Tel: +81-45-778-5875

13 Fax: +81-45-778-5497

14

15 <sup>2</sup>E-mail: [miyazawa@jamstec.go.jp](mailto:miyazawa@jamstec.go.jp)

16 The Japan Agency for Marine-Earth Science and Technology, Environmental Variability Prediction  
17 and Application Research Group, Yokohama Institute for Earth Sciences, 3173-25 Showa-machi,  
18 Kanagawa-ku, Yokohama 236-0001, Japan

19

20 <sup>3</sup>E-mail: guoxinyu@sci.ehime-u.ac.jp

21 Center for Marine Environmental Studies, Ehime University, 2-5 Bunkyo-cho, Matsuyama 790-8577,  
22 Japan

23

## 24 Abstract

25 The multi-decadal variation in ocean acidification indices in the Northwest Pacific was examined  
26 using a biogeochemical model with an operational ocean model product for the period 1993–2018. We  
27 found that ocean acidification varied regionally in the Northwest Pacific. The surface ocean (above  
28 100 m depth) underwent acidification that progressed more quickly in the subtropical region and the  
29 Kuroshio extension than in the subarctic region due to vertical mixing of the dissolved inorganic  
30 carbon (DIC) supply exceeding DIC release by air–sea exchange. Below 100 m depth, acidification  
31 and alkalization occurred in the subtropical and subarctic regions, respectively. We attribute these  
32 regional differences in acidification and alkalization to spatially variable biological processes in the  
33 upper layer and physical redistribution of DIC, both horizontally and vertically.

34

35 Keywords: biogeochemical model, Northwest Pacific, ocean acidification, ocean  
36 alkalization, JCOPE

37

## 38 1. Introduction

39 The atmospheric partial pressure of CO<sub>2</sub> (pCO<sub>2</sub>, air) has been increasing at a rate of ~1.8 parts per  
40 million by volume (ppmv) per year in recent decades as a result of human activities such as fossil fuel  
41 burning, deforestation, and cement production (Takahashi et al. 2009; IPCC 2013). During the pre-  
42 industrial period, the ocean was generally a net source of CO<sub>2</sub> emissions to the atmosphere due to in  
43 situ production and mineralization of land-derived organic matter and CaCO<sub>3</sub> precipitation. However,  
44 the increase in atmospheric CO<sub>2</sub> concentrations due to changes in land use and fossil fuel combustion  
45 has reversed the direction of the air–sea CO<sub>2</sub> flux in recent years. As a result, the majority of the ocean  
46 is now a net sink of anthropogenic CO<sub>2</sub>. However, oceanic coastal zones have changed from a sink of  
47 CO<sub>2</sub> to a source as industrial activity has increased (Mackenzie et al. 2004; Bauer et al. 2013). The  
48 present thickness of the surface ocean layer, where a fraction of the anthropogenic CO<sub>2</sub> emissions is  
49 stored, is estimated to be on the order of a few hundred meters (Mackenzie et al. 2004).

50 The major sink zones for atmospheric CO<sub>2</sub> are located at latitudes 40°–60°N and 40°–60°S  
51 (Takahashi et al. 2002, 2009, 2014; Yasunaka et al. 2013). Conversely, intense CO<sub>2</sub> source areas  
52 include the eastern equatorial Pacific and the northwestern Arabian Sea (Takahashi et al. 2002, 2009,  
53 2014). The tropical Atlantic, Indian Ocean, and northwest subarctic Pacific are also prominent CO<sub>2</sub>  
54 source areas (Takahashi et al. 2002, 2009, 2014). In the sink zones (40°–60°N and 40°–60°S), low-  
55 pCO<sub>2</sub> waters are rapidly formed by the juxtaposition of the cooling of warm waters with biological  
56 drawdown of pCO<sub>2</sub> in the nutrient-rich subpolar waters, while high wind speeds over these low-pCO<sub>2</sub>  
57 waters further accelerate CO<sub>2</sub> uptake (Takahashi et al. 2002).

58 Chemical variables related to the carbonate cycle are currently being monitored in several ongoing  
59 ocean projects to determine whether the rate of ocean acidification can be identified from changes in  
60 pH and other variables in the open ocean (Gonzalez-Davila et al. 2007; Bates 2007; Dore et al. 2009;  
61 Olafsson et al. 2009; Midorikawa et al. 2010; Bates et al. 2014; Wakita et al. 2017). In the Northwest  
62 Pacific, Midorikawa et al. (2010) estimated surface  $\text{pH}_{25}$  trends from a 25-year time-series of carbonate  
63 parameters along the  $137^\circ\text{E}$  line south of  $35^\circ\text{N}$  using repeat-observation data from the Japan  
64 Meteorological Agency (JMA). The results revealed that  $\text{pH}_{25}$  decreased by  $0.0013 \pm 0.0005 \text{ yr}^{-1}$  in  
65 summer and  $0.0018 \pm 0.0002 \text{ yr}^{-1}$  in winter during 1983–2007. Wakita et al. (2017) examined  
66 variations in ocean acidification during winter in the subarctic Northwest Pacific Ocean from 1997 to  
67 2011 (K2:  $47^\circ\text{N}$ ,  $160^\circ\text{E}$ ; KNOT:  $44^\circ\text{N}$ ,  $155^\circ\text{E}$ ) and found that  $\text{pH}_{\text{insitu}}$  in the winter mixed layer  
68 decreased at a rate of  $-0.0011 \pm 0.0004 \text{ yr}^{-1}$ , which was slower than the general mean rate in the  
69 subtropical region ( $-0.002 \text{ yr}^{-1}$ , Midorikawa et al. 2010). Their results also revealed a decline in  $\text{pH}_{\text{insitu}}$   
70 at a rate of  $-0.0051 \pm 0.0010 \text{ yr}^{-1}$  between 200 and 250 m below the mixed layer corresponding to the  
71 density zone of  $26.9\sigma_\theta \text{ kg m}^{-3}$  during their study period, which was larger than any previously reported  
72  $\text{pH}_{\text{insitu}}$  decline in the surface layer in the open North Pacific. Chen (2017) examined historical records  
73 of  $\text{pH}_{\text{insitu}}$  in the Japan Sea, calculated from reconstructions of dissolved inorganic carbon (DIC) and  
74 total alkalinity (ALK) determined from dissolved oxygen ( $\text{DO}_2$ ) concentrations measured by the  
75 Winkler method with precision and accuracy of approximately  $\pm 0.3 \mu\text{mol/kg}$  (Wong et al. 2009). The  
76 study showed that the rate of ocean acidification was different for each depth, with the rate being twice

77 as high in the subsurface layer (300–400 m depth) than in the surface layer.

78 Analyses using measurements of  $\text{pH}_{\text{insitu}}$  ( $\text{pH}_{25}$ ) are limited due to their patchy distributions in time  
79 and space. The current understanding of ocean acidification relies on pH measurements from time-  
80 series at several fixed monitoring stations (Gonzalez-Davila et al. 2007; Bates 2007; Dore et al. 2009;  
81 Midorikawa et al. 2010; Olafsson et al. 2009; Bates et al. 2014; Wakita et al. 2017). A robust three-  
82 dimensional view of basin-scale ocean acidification, however, has not yet been captured.

83 Several biogeochemical models of the CMIP5 projects (Coupled Model Intercomparison Project  
84 Phase 5) (e.g., Mackenzie et al. 2004; Watanabe et al. 2011) contain supplementary parameters related  
85 to ocean acidification indices (i.e., pH), such as DIC and ALK. Despite challenges in early model  
86 experiments, the results from these experiments predicted that ocean acidification in the North Polar  
87 region would spread gradually to the south along the eastern Pacific coast, and progress into ocean  
88 basins for the next 100 years (Kleypas et al. 2006). The long-term progress of the marine carbon cycle  
89 with global ocean circulation in the deeper layers simulated by the CMIP5 models could involve a lot  
90 of uncertainty in detail (Maekenzie et al. 2004; Kleypas et al. 2006; Watanabe et al. 2011). This  
91 uncertainty could be primarily due to a lack of understanding of the climatology of the parameters  
92 related to the marine carbon cycle, especially in the deeper layers (Takahashi et al. 2002, 2009, 2014;  
93 Yasunaka et al. 2013), as well as coarse horizontal and vertical resolutions that failed to represent  
94 advection effects generated by ocean currents.

95 The JCOPE model (Japan Coastal Ocean Predictability Experiment;

96 <http://www.jamstec.go.jp/jcope/>) is an operational eddy-resolving ocean physical model (Miyazawa et  
97 al. 2017) that incorporates observational data from floats, satellites, and shipboard measurements, and  
98 is responsible for reproducing the reanalysis model product from 1993–2018 in the Northwest Pacific  
99 (Miyazawa et al. 2019). JCOPE\_EC is a biogeochemical model that includes the carbon cycle and  
100 parameters related to ocean acidification indices, and was developed and run on the physical  
101 background of the JCOPE Northwest Pacific model outputs (Ishizu et al. 2019, 2020). The results from  
102 these model runs suggest that the model reliably reproduces distributions of the biogeochemical  
103 parameters (DIN, DIC, ALK) on a seasonal scale (Ishizu et al. 2019, 2020).

104 This study investigates long-term (multi-decadal) variation in the inorganic marine carbon cycle  
105 using JCOPE\_EC. Using the model outputs, we examine multi-decadal variations in DIC, ALK and  
106 ocean acidification indices ( $\text{pH}_{\text{insitu}}$ ,  $\text{pH}_{25}$ ,  $\Omega_{\text{arg}}$ ) in the Northwest Pacific, and compare them with  
107 available observational data. In Section 2, details of the model and data are described. Section 3  
108 includes the results of the multi-decadal simulations of the ocean acidification indices and a  
109 comparison between available observation data and model outputs. In Section 4, air–sea  $\text{CO}_2$  fluxes  
110 and possible mechanisms of the multi-decadal variation in ocean acidification are discussed. Finally,  
111 the conclusions are provided in Section 6.

112

## 113 2. Model and data

114 JCOPE\_EC (Ishizu et al. 2019, 2020) is an off-line tracer model driven by physical processes

115 simulated by an operational eddy-resolving ocean general-circulation model (JCOPE2M; Miyazawa  
116 et al. 2017, 2019), based on the Princeton Ocean Model with a generalized sigma coordinate (Mellor,  
117 2001). The model is a three-dimensional regional model covering the Northwest Pacific (10.5°–62°N,  
118 108°–180°E) with a horizontal resolution of 1/12 of a degree (4.4–9.1 km) and 46 active vertical levels.  
119 The set-up of the carbon cycle in the model is the same as the general form of OCMIP protocol (Orr  
120 et al. 2005). The JCOPE\_EC model calculates pCO<sub>2</sub> based on temperature, salinity, DIC, and ALK  
121 (Ishizu et al. 2019, 2020). The atmospheric CO<sub>2</sub> values are given by the empirical formula created  
122 based on the observational data (Ishizu et al. 2019). Reproducibility of the model output above 500 m  
123 depth has been demonstrated previously for the seasonal carbon cycle (Ishizu et al. 2020).

124 The model was driven by forcing from daily oceanic (JCOPE2M) and six-hourly atmospheric  
125 (NCEP/NCAR) reanalysis data from 1993 to 2018, yielding an analysis period of 26 years. The initial  
126 concentrations of phytoplankton were set to 0.1 and 0.0 mmol m<sup>-3</sup> for depths above and below 150 m,  
127 respectively. The initial zooplankton concentrations were set to 10% of the phytoplankton  
128 concentrations. The initial detritus concentration was set to 0.0 mmol m<sup>-3</sup>. The variables, dissolved  
129 inorganic nitrogen (DIN), phosphate (DIP), and DIC were initialized using the monthly climatology  
130 for January, and ALK was initialized using the annual climatology at the beginning of the model run  
131 (Ishizu et al. 2019, 2020). The boundary conditions were set using the monthly climatology for DIN,  
132 DIP, and DIC and the annual climatology for ALK (Ishizu et al. 2019, 2020).

133 The temporal variations in DIC calculated from the model were relatively large between 1993 and

134 1998 (Appendix A), but became stable after 1999. We therefore regard the years from 1993–1998 as a  
135 spin-up period and only use the model outputs after 1999 for the analysis (Figs 1–5, 8–13, Table 1).

136 Temperature, DIC, and ALK drive the annual variation in ocean acidification indices, but DIC exerts  
137 the strongest influence on ocean acidification. We used observational profiles to confirm that changes  
138 in  $\text{pH}_{25}$  are mainly linked with changes in DIC (not shown). To validate the reproducibility of long-  
139 term variation in ocean acidification in the model, we compared observations of DIC from 1999–2018  
140 with the model outputs along the same section (line 165°E) in Section 3.3. There are no available  
141 observations of ALK that encompass at least a 10-year span within the target period from 1999 to 2018.

142 The observational data for 2017 and 2018 along line 165°E were obtained from JMA (Japan  
143 Meteorological Agency; [https://www.data.jma.go.jp/kaiyou/db/vessel\\_obs/data-  
144 report/html/ship/ship.php](https://www.data.jma.go.jp/kaiyou/db/vessel_obs/data-report/html/ship/ship.php)), and the data for 1992, 2000, and 2006 were obtained from PACIFICA  
145 (PACIFIC ocean Interior Carbon; [https://climatedataguide.ucar.edu/climate-data/pacifica-pacific-  
146 ocean-interior-carbon](https://climatedataguide.ucar.edu/climate-data/pacifica-pacific-ocean-interior-carbon)). The monitoring data at line 165°E in the Northwest Pacific were used for the  
147 analysis described in Section 3.3.

148

## 149 3. Results

### 150 3.1 Long-term variation in ocean acidification indices represented by JCOPE\_EC

151 We define the rate of change in parameter  $C(x, y, z, t)$  from 1999–2018 using the following  
152 equation:

$$C(x, y, z, 2018 - 1999) = (\langle C(x, y, z, 2018) \rangle - \langle C(x, y, z, 1999) \rangle) / (2018 - 1999 + 1)$$

(1)

where  $\langle \rangle$  denotes the annual mean of the parameter for the specified year. The rates of change in the ocean acidification indices represented by JCOPE\_EC reveal regional differences in ocean acidification (Fig. 1). Ocean acidification was evident in the surface layer, but alkalization was also detected in some areas, especially below 100 m depth. The surface  $\text{pH}_{\text{insitu}}$  ( $\text{pH}_{25}$  and  $\Omega_{\text{arg}}$ ) declined within  $0.002 \text{ yr}^{-1}$  over most of the study area, suggesting a progression towards ocean acidification (Fig. 1a, e, i). In the lower latitudes of the subtropical region ( $20^{\circ}$ – $35^{\circ}\text{N}$ ), ocean acidification was stronger in the surface and subsurface layers (Fig. 1a–c). Strong increases in  $\text{pH}_{\text{insitu}}$  (indicating alkalization) were found in the northern side of the Japan Sea, and in the offshore surface region of the northern Japanese coast ( $35^{\circ}$ – $40^{\circ}\text{N}$ ,  $140^{\circ}$ – $150^{\circ}\text{E}$ ; Fig. 1a, e, i). The rate of change in  $\text{pH}_{\text{insitu}}$  was more intense at greater depths (Fig. 1a–d). The progression towards acidification and/or alkalization strengthens with increasing depth and spreads to the south: the rate of change in  $\text{pH}_{\text{insitu}}$  is within  $-0.002 \text{ yr}^{-1}$  in the surface region south of  $30^{\circ}\text{N}$ , but the  $\text{pH}_{\text{insitu}}$  values from  $-0.002$  to  $-0.004 \text{ yr}^{-1}$  spread at the depth of 100 m (Fig. 1b). Evidence of strong acidification is found in the southern area around  $15^{\circ}$ – $20^{\circ}\text{N}$  at depths of 200 and 500 m (Fig. 1c, d). Alkalization spreads southward across the Kuroshio Extension below the subsurface (Fig. 1c–d). Vertical sections of  $\text{pH}_{\text{insitu}}$  along the  $165^{\circ}\text{E}$  line (Fig. 2) reveal a progression towards acidification within  $0.002 \text{ yr}^{-1}$  in the surface, and a strong progression towards acidification in the subtropical region south of  $25^{\circ}\text{N}$  at depths of 200–600 m.

172 Alkalinization occurs north of 25°N, especially in the subarctic region (Fig. 2a). Strong acidification  
173 or alkalinization is found below 200 m depth. Areas of enhanced acidification and alkalinization are  
174 found in the regions of 15°–25°N and 40°–45°N, respectively, along the vertical section of line 165°E  
175 (Fig. 2a).

176 Patterns of acidification and alkalinization revealed by  $\text{pH}_{25}$  and  $\Omega_{\text{arg}}$  agree with those suggested  
177 by  $\text{pH}_{\text{insitu}}$  (Fig. 1e–l). Ocean acidification is found in the surface layer, while strong contrasts in  
178 acidification and alkalinization are evident in the deeper layers, especially at depths of 200–800 m (Fig.  
179 2b, c).

180

### 181 3.2 Long-term variations in temperature, salinity, DIC, and ALK

182 The variation in ocean acidification indices is driven by temperature, salinity, DIC, and ALK (Ishizu  
183 et al. 2019). Temperature shows an increase across most of the study region in the surface waters (Fig.  
184 3a). Temperature increased by 0.1 °C in the subarctic region (30°–40°N, 140°–170°E) and decreased  
185 by 0.1 °C in the area south of Japan (30°–31°N, 130°–140°E; Fig. 3a). The strong increase in the  
186 subarctic region (30°–40°N, 140°–170°E) coincides with the polar front area (Isoguchi et al. 2006; Fig.  
187 3a). On the other hand, the strong decrease in temperature observed in the area south of Japan is a  
188 consequence of the large Kuroshio meander in 2018. We also see a large increase in temperature in the  
189 Okhotsk Sea and the Pacific area north of 50°N (Fig. 3a). A moderate temperature increase is observed  
190 north of 50°N below the surface. On the other hand, the temperature increase becomes prominent

191 toward south from 50°N, particularly near the boundary between the subtropical region and the  
192 Kuroshio Extension (Fig. 3a–d). We note that long-term forcing effects, such as global warming and  
193 consequent ocean acidification, may influence the large-scale horizontal behavior of the change rate.  
194 Conversely, some of the locally intensive variations could be affected by year-to-year variations related  
195 to interannual variations in ocean currents, such as the large Kuroshio meander.

196 The distribution of the change rate of salinity (Fig. 3e–h) matches the pattern of the temperature  
197 change rate (Fig. 3a–d), although changes in salinity have a weak influence on ocean acidification.  
198 The distributions of potential density change rate match those of temperature and salinity, although the  
199 increases in the density change rate are seen where decreases in temperature and salinity occur, and  
200 vice versa (Fig. 3i–l).

201 DIC basically increases in the surface (Fig. 4a). However, the distributions of DIC change are not  
202 uniform (Fig. 4a–b). The strongest DIC increase in the surface waters is found in the subtropical region  
203 (18°–35°N, 130°–180°E), the southeast area of the Japan Sea (30°–40°N, 130°–140°E), and the East  
204 China Sea (30°–40°N, 120°–125°E; Fig. 4a). On the other hand, local DIC decreases at the surface are  
205 found in the Okhotsk Sea, the Japan Sea, and the eastern offshore waters of Hokkaido (35°–40°N,  
206 140°–160°E; Fig. 4a). The DIC decrease becomes stronger below 100 m depth and spreads to the south.  
207 A DIC increase is seen in the southern subtropical region (Fig. 4b–d). The strongest DIC increase  
208 occurs at 200 m depth in the region between 15°–25°N and 120°–160°E, and the strongest decrease in  
209 the area north of 40°N (Fig. 4c). The vertical distribution of DIC along the 165°E line (Fig. 5a)

210 indicates that DIC increases in the surface waters and in the upper 800 m in the southern part from  
211 20°N. DIC decreases near the boundary between the subtropical and the subarctic regions in the depth  
212 range between 400 and 1000 m (Fig. 5a). The DIC decrease spreads below 200 m depth between 35°  
213 and 50°N, with the strongest decrease occurring in the depth range of 600–800 m near 45°N in the  
214 subarctic region (Fig. 5a).

215 The change rate of ALK between 1993 and 2018 is within 1  $\mu\text{mol/kg/yr}$  (Figs. 4e–h, 5b), which is  
216 weaker than that of DIC (Figs. 4a–d, 5a). A weak decrease of ALK occurs in the Okhotsk Sea and  
217 along the Kamchatka Peninsula in the depth range of 0–500 m (Fig. 4e–h). The weak increase of ALK  
218 spreads more broadly in the subtropical region along the vertical section (Fig. 5b). The ALK decrease  
219 in the subarctic region at 200 m depth connects with the large decrease in the Okhotsk Sea (Fig. 4h).  
220 The patterns in ALK variation generally agree with those of DIC (Figs. 4, 5).

221

### 222 3.3 Comparison between observational DIC data and simulation results

223 Long-term variations in DIC ( $\mu\text{mol/kg/yr}$ ) from observational data along line 165°E (Fig. 6) reveal  
224 patterns that are consistent with the simulation results. Although the DIC observations contain seasonal,  
225 interannual, and bi-decadal variability due to temporal variations in the collection of the DIC  
226 measurements (Cook et al. 1997; Bionde et al. 2001; Yasuda et al. 2008), the tendency of the DIC  
227 increase spreads with increasing depth in the subtropical region (15°–30°N) and the tendency of the  
228 DIC decrease spreads partially and/or throughout the depth in the subarctic region (35°–48°N). A

229 fraction of the area that contains the DIC increase resides in the subarctic region (Fig. 6a, b, d, e). The  
230 areas of DIC increase in the subarctic region are located near the surface layer or close to the Kuroshio  
231 Extension (35°–40°N; Fig. 6).

232 Comparing the vertical distribution of the simulated increases and decreases in DIC (Figs. 4a–d, and  
233 5) with that of the DIC observations (Fig. 6), we find that the area of alkalinization residing in the  
234 subtropical region below the subsurface in the model outputs (Figs. 4a–d, 5a) is not basically found in  
235 the observations (Fig. 6). The area of DIC decrease below the subsurface in our model is wider than  
236 the area of DIC decrease in the observations (Figs. 4a–d, 5a, 6). A vertical section of the DIC difference  
237 between 1995 and 2018 may include effects of the spin-up process (Fig. 7), but the agreement between  
238 distributions of DIC changes from 1995 to 2018 (Fig. 7) and the observations appears to be better than  
239 that between DIC changes from 1999 to 2018 (Fig. 5a) and the observations.

240

## 241 4. Discussion

### 242 4.1 Comparison with previous observational results

243 Midorikawa et al. (2010) found that ocean acidification occurs in the surface waters of the  
244 subtropical region. The authors estimated  $\text{pH}_{25}$  changes of  $0.0013 \pm 0.0005 \text{ yr}^{-1}$  for summer and  $0.0018$   
245  $\pm 0.0002 \text{ yr}^{-1}$  for winter for surface waters in the subtropical region along the 137°E line. Our model  
246 estimates that the surface  $\text{pH}_{25}$  changes at a rate of  $0.0019 \text{ yr}^{-1}$  at 30°N, 137°E, which indicates  
247 progression of acidification and is consistent with the estimate of Midorikawa et al. (2010).

248 In the northern region of our study area, Wakita et al. (2013) estimated a change in ocean  
249 acidification at a rate of  $0.0011 \pm 0.0004 \text{ yr}^{-1}$  in the surface mixed layer, and at a rate of  $0.0051 \pm$   
250  $0.0010 \text{ yr}^{-1}$  in the 200–250 m depth range at the K2 station (47°N, 160°E). In the Japan Sea, Chen et  
251 al. (2017) estimated that ocean acidification progressed at rates of  $-0.0038$ ,  $-0.0027$ , and  $-0.0021 \text{ yr}^{-1}$   
252 <sup>1</sup> at 300, 400, and 500 m depth, respectively. Our simulation result, however, suggests a progression  
253 towards alkalization above 100 m, and an even stronger progression towards alkalization below  
254 100 m in the northern regions of the Northwest Pacific and Japan Sea (Fig. 1).

255 Several research programs are aiming to measure parameters related to ocean acidification indices.  
256 The World Ocean Circulation Experiment (WOCE) includes cruise lines that contain the annual  
257 observations from some of these programs. The Ocean Carbon and Acidification Data Portal is  
258 currently organizing a system for gathering the observational data and making it publicly available  
259 ([https://www.nodc.noaa.gov/oads/stewardship/data\\_portal.html](https://www.nodc.noaa.gov/oads/stewardship/data_portal.html)). This system should enable access to the  
260 observational data under international control. When additional data are made available, we may have  
261 a better three-dimensional view of acidification and alkalization in the global ocean.

262

## 263 4.2 Air–sea CO<sub>2</sub> flux

264 The lack of agreement between the simulated long-term DIC changes and the observations may be  
265 due to the pCO<sub>2</sub> calculation scheme applied to JCOPE\_EC. Several studies have noted the poor  
266 agreement between the measured and modeled pCO<sub>2</sub>, which is calculated from DIC and ALK (Orr and

267 Epitalon, 2015; Valsala and Maksyutov 2015; Ishizu et al. 2019, 2020). This poor agreement likely  
268 influences the reproducibility of the simulated absorption of CO<sub>2</sub> into the ocean. In our target region,  
269 the calculated oceanic pCO<sub>2</sub> is larger than the measurements in most areas. Accordingly, the modeled  
270 absorption rate is expected to be smaller than the true absorption rate, and the area of DIC increase in  
271 the model may be smaller than the area in the observations (Figs. 4a–d, 5a, 6). The horizontal  
272 distribution of annual air–sea CO<sub>2</sub> fluxes (Fig. 8) reveals that the majority of the Pacific plays a role  
273 in CO<sub>2</sub> emissions, except for marginal seas which are sinks of CO<sub>2</sub>. Some parts of the Northwest  
274 Pacific also appear to play a role in the active uptake of CO<sub>2</sub>.

275 The annual emission rate of CO<sub>2</sub> from ocean to atmosphere (Fig. 9) gradually decreased from 1999  
276 to 2018 in subarctic waters, the Kuroshio Extension, and the subtropical region. The regressions  
277 calculated from the statistical regression analysis in the subarctic region, the Kuroshio extension, and  
278 the subtropical region were 0.0015, 0.0015, and 0.0006 Pg C yr<sup>-1</sup>, respectively. The p-values for each  
279 region were  $6.9 \times 10^{-5}$ ,  $5.5 \times 10^{-2}$ , and  $1.4 \times 10^{-1}$ , respectively. Since all of the regressions are positive,  
280 the CO<sub>2</sub> release in the subarctic, the Kuroshio extension, and the subtropical region decreases with  
281 increasing atmospheric CO<sub>2</sub> concentration. Only the p-values in the Kuroshio Extension and  
282 subtropical region are greater than 0.05, indicating that the statistical regression in the subarctic region  
283 is not reliable. Large variability in air–sea CO<sub>2</sub> fluxes in the Kuroshio Extension (Fig. 9) is likely  
284 driven by the strong eddy activity in that region.

285

286 4.3 Possible mechanisms of long-term changes in ocean acidification and alkalization  
287 in the Northwest Pacific represented by JCOPE\_EC

288 We decided to further examine the DIC increase in the surface region of the Northwest Pacific and  
289 the DIC distribution in the subsurface waters between the subtropical region and the subarctic region,  
290 where the processes controlling acidification and alkalization are different (Figs. 1a–d, 4a–d). To  
291 accomplish this, we calculated the mean balances of the DIC variation terms generated by physical  
292 and biological processes, as follows (Ishizu et al. 2019):

$$\frac{\partial[DIC]}{\partial t} = \left[\frac{\partial[DIC]}{\partial t}\right]_A + \left[\frac{\partial[DIC]}{\partial t}\right]_{xy\_dif} + \left[\frac{\partial[DIC]}{\partial t}\right]_{z\_dif} + \left[\frac{\partial[DIC]}{\partial t}\right]_{Bio} + \left[\frac{\partial[DIC]}{\partial t}\right]_{air-sea}, \quad (2)$$

293 where the subscripts *A*, *xy\_dif*, *z\_dif*, *Bio*, and *air-sea* represent the time derivatives of DIC induced  
294 by advection, horizontal diffusion (i.e., horizontal mixing), vertical mixing, biological processes, and  
295 air-sea CO<sub>2</sub> exchange, respectively (positive *air-sea* values indicate a transfer of CO<sub>2</sub> from air to sea).

296 We refer to these as the “DIC variation terms”, and the DIC variations induced by air-sea CO<sub>2</sub>  
297 exchange are only included for the surface level. The total DIC variation term on the left side of Eq.  
298 (2) is the sum of all terms on the right-hand side of the equation. Note that the influencing terms were  
299 calculated with the DIC calculations in the simulation, but the outputs were sampled at one time-step  
300 per day. The averaged terms for the period of 1999–2018 were analyzed. The temporally averaged total  
301 variation term  $\frac{\partial[DIC]}{\partial t}$  (left side of Eq. 2) is thus not the same as the change rate term (Eq. 1), which  
302 is calculated from the difference between the annual mean for 1999 and 2018.

303 The horizontal distributions of the DIC variation terms in Eq. (2) are shown in Figs. 10–12, while

304 Fig. 13 displays depth-dependent variation in the DIC variation terms along the 165°E line at 20°, 30°,  
305 40°, and 50°E. The balances at the surface (Fig. 10a–f) indicate that air–sea exchange is generally  
306 balanced by vertical mixing (Figs. 10c, e, 13a–d), and that biological processes drive the DIC increase  
307 in the Kuroshio Extension and the subtropical region as well as the DIC decrease in the subarctic region  
308 north of 50°N (Figs. 10d, 13a–d). The DIC increase in the Kuroshio Extension and the subtropical  
309 region can be attributed to remineralization, which occurs due to the spreading of detritus originating  
310 from zooplankton (not shown). The DIC decrease in the subarctic region is due to photosynthesis. The  
311 balance of the yearly DIC variations terms along the 165°E line in the subtropical region and the  
312 surface region of the Kuroshio Extension (Fig. 13a, b, e) suggests that the DIC supply, which is  
313 primarily controlled by vertical mixing, surpasses the DIC release by air-sea exchange. As the depth  
314 increases (Figs. 10g–k, 11, 12, 13e–s), the DIC time variations are primarily driven by vertical mixing,  
315 biological processes and/or advection. Vertical mixing transports DIC from deeper layers to the surface  
316 waters (above 50 m) in the Kuroshio Extension and the subarctic region (Fig. 10c, g, j, 13e, f). At 100  
317 m, the negative DIC values are due to photosynthesis, which consumes DIC in the subtropical region  
318 (Fig. 11d). The positive DIC values in the subarctic region north of 40°N (Fig. 11d), however, indicate  
319 production of DIC due to remineralization. Such latitudinal differences between the subtropical region  
320 and the subarctic region are therefore due to biological processes (Fig. 11d, i), and can be linked with  
321 latitudinal differences in the depth of the chlorophyll maximum in the Northwest Pacific (Sauzede et  
322 al. 2015; Ishizu et al. 2020). Below 200 m (Figs. 11f–j, 12), biological processes become less important

323 in driving DIC variations. Instead, advection is largely responsible for DIC variations by way of  
324 vertical mixing (Fig. 11f, h, j, 13m–s). Horizontal mixing does not appear to play an important role in  
325 driving lateral or depth-dependent DIC variations across this study area (Fig. 10–12).

326 Observations of DIC (Fig. 5) suggest that ocean acidification in the subtropical region above 200–  
327 500 m has advanced more rapidly than the subarctic region. Results from the simulation suggest that  
328 vertical mixing balances the ejection of DIC at the surface despite CO<sub>2</sub> release to the atmosphere. This  
329 likely causes acidification to proceed faster in the subtropical region than in the subarctic region (Fig.  
330 4a). The observations also raise the possibility of alkalinization in the subarctic region below 100 m.  
331 The analysis of the model products also suggests that the supply from DIC transport in the subarctic  
332 region below 100 m is less than that of the upper layers due to vertical mixing (Fig. 10–13, Fig.13a, h,  
333 l, p). This process is responsible for the DIC decrease in the subarctic region (Fig. 4b–d, 5a, 10f, 10k,  
334 11e, 11j, 13c–d, 13g–h), and likely leads to alkalinization in the shallow waters there (Fig. 1b–d, 1f–h,  
335 1j–l, 10j, 10k, 11e). DIC is transported to the Kuroshio Extension and the subtropical region below  
336 200 m (Fig. 11f, 12a, 13 q–t, u–s). The formation and transport of several mode waters, such as the  
337 North Pacific Intermediate Water ( $\sigma_{\theta} = 26.8 \text{ kg m}^{-3}$ ; Talley 1993; Yasuda 2004; Fujii et al. 2013), occur  
338 within the 200–600 m depth range, indicating that advection of DIC is consistent with the general  
339 patterns of ocean circulation in the Northwest Pacific (Fig. 5a).

340

## 341 5. Conclusion

342 A biogeochemical model with an operational ocean product was used to examine long-term three-  
343 dimensional variation in ocean acidification indices and parameters related to ocean acidification from  
344 1993 to 2018. The model results indicate an increase in DIC and a progression towards ocean  
345 acidification over most of the surface layer, although most of the Northwest Pacific is identified as a  
346 source of CO<sub>2</sub> to the atmosphere. The results exhibit distinct contrasts between the subtropical and  
347 subarctic regions at increasing depths: ocean acidification is suggested in the subtropical region, while  
348 alkalization appears to occur in the subarctic region. The analysis of the model product indicates that  
349 ocean acidification represented by this model is strongly controlled by the physical transport of DIC  
350 that occurs due to ocean circulation, with biological activity. Historical DIC observations in the  
351 Northwest Pacific show similar patterns across the Kuroshio Extension region. The analysis of the  
352 model product indicates that ocean acidification represented by this model is primarily driven by  
353 vertical mixing and air-sea exchange at the surface. In the deeper layers below 100 m, we see contrasts  
354 of ocean acidification and alkalization in the subtropical region and the subarctic region, where  
355 biological processes with the modulation of the physical processes such as advection, horizontal  
356 transport, and vertical diffusion are strongly impacted.

357 Although our model experiment does not distinguish between DIC changes due to ocean circulation  
358 and those due to increased injection of atmospheric CO<sub>2</sub> as a consequence of global warming, our  
359 model experiment does allow for the possibility that ocean acidification in the subtropical gyre south  
360 of the Kuroshio Extension proceeds faster than that in the subarctic region. CO<sub>2</sub> could be injected in

361 the Kuroshio Extension region in winter by subduction processes (not shown), and the injected CO<sub>2</sub> in  
362 the subsurface and deeper layers may gradually reach the surface, with possibility of more rapid  
363 transport to the surface in the subtropical region. Our simulation results suggest that the concentrations  
364 of DIC (CO<sub>2</sub>) in the subtropical region and alongshore coastal area south of 40°N in the Northwest  
365 Pacific may increase in the future. This has strong implications for ocean acidification, and thus  
366 demands planning for such a scenario.

367

## 368 Acknowledgements

369 We acknowledge support from the Sasakawa Peace Foundation of the Ocean Policy Research Institute  
370 (OPRI-SPF). This study is part of the Japan Coastal Ocean Predictability Experiment (JCOPE)  
371 promoted by the Japan Agency for Marine-Earth Science and Technology (JAMSTEC).

372

## 373 Appendix

### 374 A. Spin-up processes

375 The averaged DIC time variations in the subarctic region, the Kuroshio Extension, and the  
376 subtropical region from 1993 to 2008 were calculated in the surface (0–100 m), subsurface (100–500  
377 m), middle (500–1000 m) and deeper (1000–2000 m) layers. The DIC time variations in the surface  
378 layer (Fig. Aa) fluctuate more widely than those in the deeper layers (Fig. Ab–d). In the subsurface  
379 layer (Fig. Ab), the DIC values decrease in the subarctic region, but increase in the Kuroshio Extension  
380 and the subtropical region. In the layers deeper than 500 m (Fig. Ac–d), a widespread decrease in DIC

381 is observed. The rate of DIC change gradually slows with time, and the fluctuations become more  
382 moderate, except for in surface waters (Fig. Aa). Using this time-series of DIC from 1993 to 2018, we  
383 define the spin-up process as the model output prior to 1999.

384

385 Funding: We acknowledge financial support from the Sasakawa Peace Foundation of Ocean Policy  
386 Research Institute.

387 Conflicts of interest/Competing interests: The authors declare no conflict of interest.

388 Ethics approval: Not applicable.

389 Consent to participate: Not applicable.

390 Consent for publication (include appropriate statements): Not applicable.

391 Availability of data and material (data transparency): Not applicable.

392 Authors' contributions: Conceptualization, YM, Methodology, MI and YM; Validation, MI and YM,  
393 Writing-Original Draft Preparation, MI; Writing-Review and Editing, MI and YM; Visualization,  
394 MI; Supervision, YM and XG; Project administration, YM; Funding Acquisition, YM.

## 395 References

- 396 1. Bates, N. R.; Interannual variability of the ocean CO<sub>2</sub> sink in the subtropical gyre of the North  
397 Atlantic Ocean over the last 2 decades, *J. Geophys. Res.*, **2007**, 112, C09013,  
398 doi:10.1029/2006JC003759
- 399 2. Bates, N. R.; Astor, Y. M.; Church, M. J.; Currie, K.; Dore, J. E.; Gonzalez-Davila, M.; Lorenzoni,  
400 L.; Muller-Karger, F.; Olafsson, J.; Santana-Casiano, J. M.; A time-series view of changing surface  
401 ocean chemistry due to ocean uptake of anthropogenic CO<sub>2</sub> and ocean acidification,  
402 *Oceanography*, **2014**, 27(1): 126-141, <http://dx.doi.org/10.5670/oceanog.2014.16.2014>.
- 403 3. Bauer, J. F.; Cai, W. J.; Raymond, P. A.; Bianchi, T. S.; Hopkinson, C. H.; Pierre, A.; Regnier, P.;  
404 The changing carbon cycle of the coastal ocean, *Nature*, **2013**, 504, 61–70,  
405 doi:10.1038/nature12857.
- 406 4. Biondi, F., Gershunov, A., Cayan, R. D.; North Pacific decadal climate variability since 1661,  
407 *Journal of Climate*, **2001**, 14, 5–10.
- 408 5. Chen, C. T. A.; Lui H-K.; Hsieh, C-H.; Yanagi, T.; Kosugi, N.; Ishii, M.; Gong, G-C. Deep oceans  
409 may acidify faster than anticipated due to global warming, *Nature communication*, **2017**, 890–  
410 895, <https://doi.org/10.1038/s41558-017-0003-y>.

- 411 6. Cook, E. R.; Meko, M. D.; Stockton W. C.; A new assessment of possible solar and lunar forcing  
412 of bidecadal drought rhythm in the western United States, *Journal of Climate*, 1997, 10, 1343–  
413 1356.
- 414 7. Even, T. L.; Weaver, A. J.; Ebe, M.: Sensitivity of the inorganic ocean carbon cycle to future climate  
415 warming in the UVic coupled model. *Atmos. Ocean*, **2004**, 42, 23–42.
- 416 8. Dore, J. E.; Lukus, R.; Sadler, D.W.; Church, M. J.; Karl, D. M.; Physical and biogeochemical  
417 modulation of ocean acidification in the central North Pacific, *Proc. Natl. Acad. Sci.*, **2009**, 106,  
418 12 235–12 240.
- 419 9. Fujii, Y.; Nakano, T.; Usui, N.; Matsumoto, S.; Tsujino, H.; Kamachi, M.; Pathways of the North  
420 Pacific Intermediate Water identified through the tangent linear and adjoint models of an ocean  
421 general circulation model, *Journal of Geophysical Research: Oceans*, **2013**, 118, 2035–2051,  
422 doi:10.1002/jgrc.20094.
- 423 10. Gonzalez-Davila, M.; Santana-Casiano, J. M.; Gonzalez-Davila, E. F. Interannual variability of  
424 the upper ocean carbon cycle in the northeast Atlantic Ocean, *Geophys. Res. Lett.*, **2007**, 34,  
425 L07608, doi:10.1029/2006GL028145.
- 426 11. Intergovernmental Panel on Climate Change (IPCC): Climate Change 2013: The Physical Science  
427 Basis. Contribution of Working Group I to the Fifth Assessment Report of the Intergovernmental  
428 Panel on Climate Change; ed. Stocker, T. F., Qin, D., Plattner, Gian-Kasper., Tignor, M. M. B.;  
429 Allen, S. K.; Boschung, J.; Nauels, A.; Zia Y.; Bex, V.; Midgley, P. M.; 1–1535 pp. Cambridge,  
430 UK: Cambridge University Press, Cambridge, United Kingdom and New York, NY, USA, 2013.
- 431 12. Ishizu, M.; Miyazawa, Y.; Tsunoda, T.; Guo, X.; Development of a biogeochemical and carbon  
432 model related to ocean acidification indices with an operational ocean model product in the North  
433 Western Pacific, *Sustainability*, **2019**, 11, 2677, doi:10.3390/su11092677.
- 434 13. Ishizu, M.; Miyazawa, Y.; Guo, X.; Tsunoda, T.; Seasonal variability in the inorganic ocean carbon  
435 cycle in the Northwest Pacific evaluated using a biogeochemical and carbon model coupled with  
436 an operational ocean model, *Climatic Change*, 2020, 1–26, doi:10.1007/s10584-020-02779-2.
- 437 14. Isoguchi, O.; Kawamura, H.; Oka, E.: Quasi-stationary jets transporting surface warm waters  
438 across the transition zone between the subtropical and the subarctic gyres in the North Pacific,  
439 *Journal of Geophysical Research*, **2006**, 111, C10003, doi:10.1029/2005JC003402.
- 440 15. Kleypas, J. A.; Feely, R. A.; Fabry, V. J.; Langdon, C.; Sabine, C. L.; Robbins, L. L.; Impacts of  
441 ocean acidification on coral reefs and other marine calcifiers: A guide for future research, report  
442 of a workshop held 18-20 April 2005, St. Petersburg, FL, sponsored by NSF, NOAA, and the US  
443 Geological Survey, 88 pp. **2006**.
- 444 16. Mackenzie, F. T.; Lerman, A.; Anderson, A. J. Past and present of sediment and carbon  
445 biogeochemical cycling models. *Biogeosciences*, 2004, 1, 11–32.
- 446 17. Mellor G. L.; An Equation of State for Numerical Models of Oceans and Estuaries, *Journal of*  
447 *Atmospheric and Oceanic technology*, **2001**, 8, 609–611.
- 448 18. Midorikawa, T.; Ishii, M., Saito, S.; Sasano, D., Kosugi, N, Motoi, T., Kamiya, H., Nkadate, A.,  
449 Nemoto, K, Inoue, H. Decreasing pH trend estimated from 25-yr time series of carbonate  
450 parameters in the western North Pacific, *Tellus*, **2010**, 62B, 649–659.
- 451 19. Miyazawa, Y.; Varlamov, M.S.; Miyama, T.; Guo, X.; Hihara, T.; Kiyomatsu, K.; Kachi, M.;  
452 Kurihara, Y.; Murakami, H. Assimilation of high-resolution sea surface temperature data into an  
453 operational nowcast/forecast system around Japan using a multi-scale three-dimensional  
454 variational scheme. *Ocean Dyn.* **2017**, 67, 713–728.
- 455 20. Miyazawa, Y.; Kuwano-Yoshida, A.; Doi, T.; Nishikawa, H.; Narazaki, T.; Fukuoka, T; Sato,  
456 K. Temperature profiling measurements by sea turtles improve ocean state estimation in the  
457 Kuroshio-Oyashio Confluence region. *Ocean Dyn.* **2019**, 69, 267-282.
- 458 21. Olafsson, J.; Olafsdottir, S. R.; Benoit-Cattin, A.; Danielsen, M.; Arnarson, T. S.; Takahashi, T.  
459 Rate of Iceland Sea acidification from time series measurements, *Biogeosciences*, **2009**, 6:2, 661–  
460 2, 668, <http://dx.doi.org/10.5194/bg-6-2661-2009>.

- 461 22. Orr, J. C.; Najjar, R.; Sabine, C.L; Joos, F.: Abiodic-HOWTO; Internal OCMIP Report;  
462 LSCE/CEA Scalay: Gif-sur-Yvette, France, 1999; 25p.
- 463 23. Orr, C. J.; Epitalon, M. J. Improved routines to model the ocean carbonate system: mocsy 2.0,  
464 Geosci. Model Dev., **2015**, 8, 485–499, [www.geosci-model-dev.net/8/485/2015doi:10.5194/gmd-](http://www.geosci-model-dev.net/8/485/2015doi:10.5194/gmd-8-485-2015)  
465 [8-485-2015](http://www.geosci-model-dev.net/8/485/2015doi:10.5194/gmd-8-485-2015)
- 466 24. Sauzede, R.; Lavigne, H.; Claustre ,H.; Schmechtig, C.; Ortenzio, D. F.; Guinet, C.; Pesant, S.  
467 Vertical distribution of chlorophyll a concentration and phytoplankton community composition  
468 from in situ fluorescence profiles: a first database for the global ocean. *Earth Syst. Sci. Data*,  
469 2015, 7, **2015**, 261–273., doi: 10.5194/essd-7-261-2015.
- 470 25. Takahashi, T.; Sutherland, C. S.; Sweeney, C.; Poisson, A.; Metzl N.; Tilbrook, B.; Bates, N.;  
471 Wanninkhof, R.; Feely, A. R.; Sabin, C.; Olafsson J.; Nojiri, Y. Global sea-air CO<sub>2</sub> flux based on  
472 climatological surface ocean pCO<sub>2</sub>, and seasonal biological and temperature effects. *Deep-Sea*  
473 *Research II*, **2002**, 49, 1601–1622.
- 474 26. Takahashi, T.; Sutherland C. S.; Wanninkhof, R.; Sweeney, C.; Feely, A. R.; Chipman, W. D.;  
475 Hales, B.; Friedrich, G.; Chaves, F.; Sbaïne, C.; Watson, A.; Bakker C. E. D.; Schuster, U.; Metzl,  
476 N.; Yoshikawa-Inoue, H.; Ishii, M.; Midorikawa, T.; Nojiri, Y.; Kortzinger, A.; Steinhoff, T.;  
477 Hoppema, M.; Olafsson, J.; Arnarson, S. T.; Tilbrook, B.; Johannessen, T.; Olsen, A.; Bellerby, R.;  
478 Wong, C. S.; Delille, B.; Bates, N. R.; de Baar J. W. H. Climatological mean and decadal change  
479 in surface ocean pCO<sub>2</sub> and net sea-air CO<sub>2</sub> flux over the global oceans. *Deep-Sea Research II*,  
480 **2009**, 56, 554–577.
- 481 27. Takahashi, T.; Sutherland, C. S.; Chipman, W. D.; Goddard, G. J.; Cheng, H.; Newberger, T.;  
482 Sweeney, C.; Munro, R. D. Climatological distributions of pH, pCO<sub>2</sub>, total CO<sub>2</sub>, alkalinity, and  
483 CaCO<sub>3</sub> saturation in the global surface ocean, and temporal changes at selected locations. *Mar.*  
484 *Chem.* **2014**, 164, 95–125.
- 485 28. Talley, L. D. Distribution and formation of North Pacific Intermediate Water, *J. Phys. Oceanogr.*,  
486 **1993**, 23, 517–537, doi: 10.1175/1520-0485.
- 487 29. Valsala, V. and Maksyutov S.: Simulation and assimilation of global ocean pCO<sub>2</sub> and air-sea CO<sub>2</sub>  
488 fluxes using ship observation of surface ocean pCO<sub>2</sub> in a simplified biogeochemical offline model,  
489 Tellus B: Chemical and physical meteorology, 62:5, 821-840, doi:10.1111/j.1600-  
490 0889.2010.00495.x.
- 491 30. Yasuda, I.; North Pacific Intermediate Water: Progress in SAGE (SubArctic Gyre Experiment)  
492 and related projects, *J. Oceanogr.*, **2004**, 60, 385–395,  
493 doi:10.1023/B:JOCE.0000038344.25081.42.
- 494 31. Yasuda, I.; The 18.6-year period moon-tidal cycle in Pacific Decadal Oscillation reconstructed  
495 from tree-rings in western North America, *Geophys. Res. Lett.*, **2008**, 36, L05605,  
496 doi:10.1029/2008GL036880.
- 497 32. Yasunaka, S.; Nojiri, Y.; Nakaoka, S.; Ono, T.; Mukai, H.; Usui, N. Monthly maps of sea surface  
498 dissolved inorganic carbon in the North Pacific: Basin-wide distribution and seasonal variation. *J.*  
499 *Geophys. Res. Oceans*, **2013**, 118, 3843–3850, doi:10.1002/jgrc.20279.
- 500 33. Wakita, M.; Watanabe, S., Honda, M.; Nagano, A.; Kimoto, K.; Matsumoto, K.; Kitamura, M.;  
501 Sasaki, K.; Kawakami, H.; Fujiki, T.; Sasaoka, K.; Nakano, Y.; Murata, A. Ocean acidification  
502 from 1997 to 2011 in the subarctic western North Pacific Ocean. *Biogeosciences*, 10, 7817–7827,  
503 2013.
- 504 34. Watanabe, S.; Hajime, T.; Sudo, K.; Nagashima, T.; Takemura, T.; Okajima, H.; Nozawa, T.;  
505 Kawase, H.; Abe, M.; Yokohata, T.; Ise T.; Sato, H.; Kato, E.; Takata, K.; Emori, S.; Kawamiya,  
506 M. MIROC-ESM 2010: Model description and basic results of CMIP5-20c3m experiments.  
507 *Geosci. Model. Dev.* **2011**, 4, 845–872, doi:10.5194/gmd-4-845-2011.

# Figures

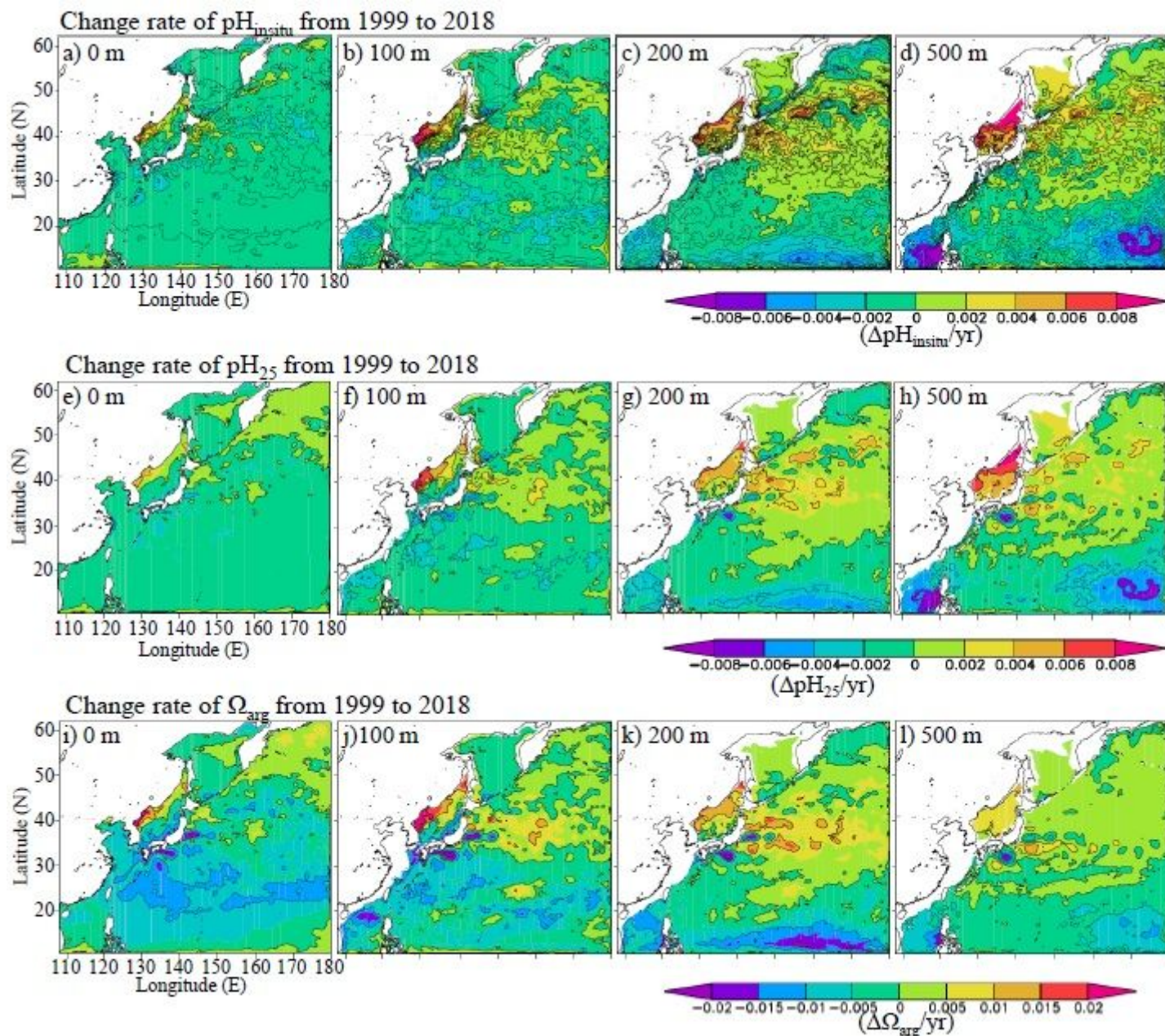
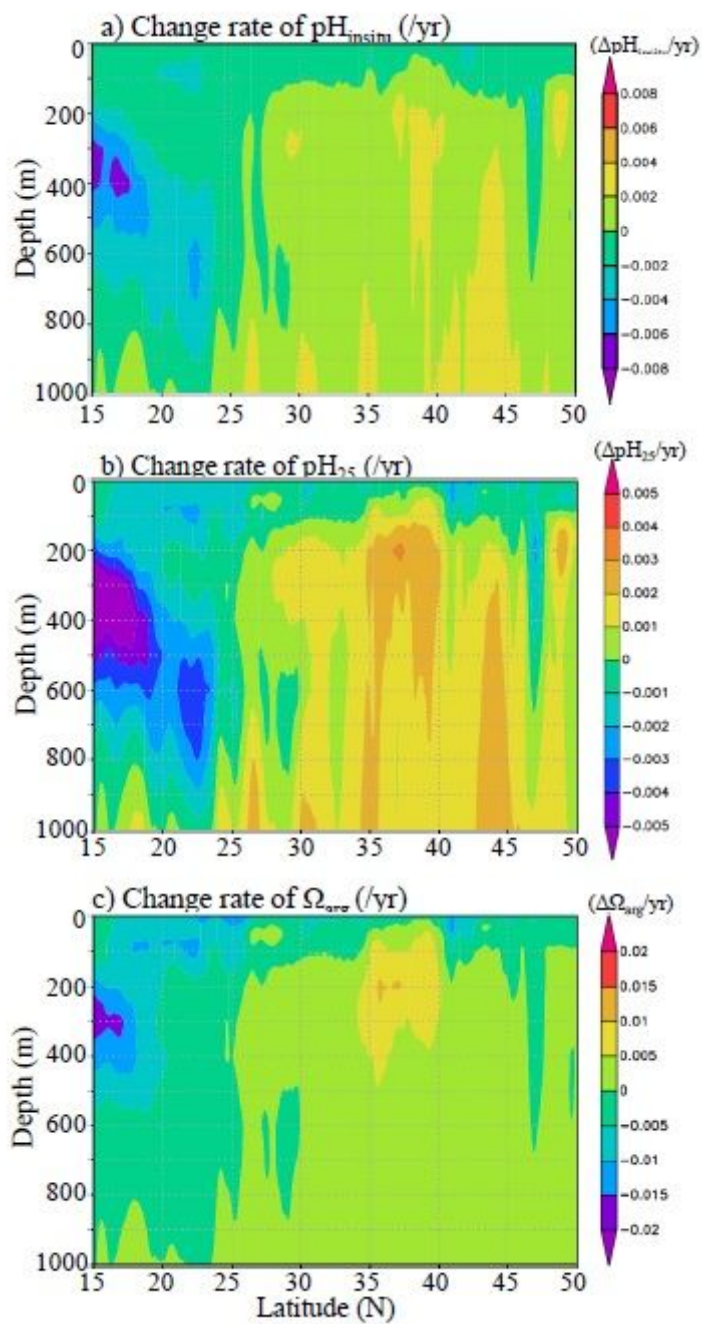


Figure 1

Horizontal distributions of change rate of  $pH_{insitu}$ ,  $pH_{25}$  and  $\Omega_{arg}$  model outputs from 1999 to 2018 at 0 m, 100 m, 200 m and 500 m depth, respectively. The annual values in 1999 are subtracted from that in 2018.



**Figure 2**

Vertical sections of change rate of motel outputs in  $\text{pH}_{\text{insitu}}$ ,  $\text{pH}_{25}$  and  $\Omega_{\text{arg}}$ , respectively, from 1999 to 2018. The annual values in 1999 are subtracted from that in 2018. Density contours in a and b are drawn for the data in 1999 and 2018, respectively.

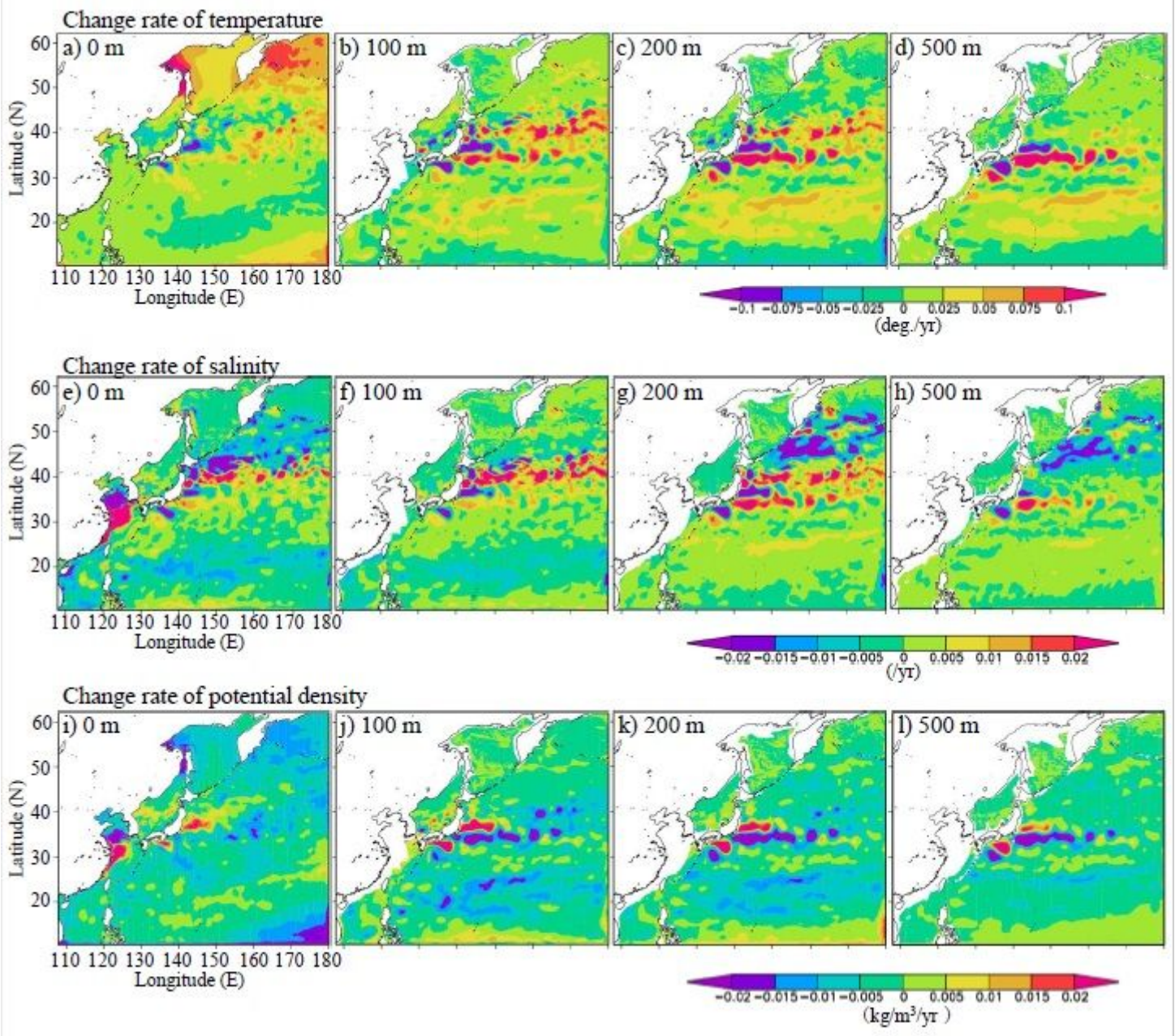


**Figure 3**

Horizontal distributions of change rate of temperature, salinity and potential density of model outputs from 1999 to 2018 at 0 m, 100 m, 200 m and 500 m depth, respectively. The annual values in 1999 are subtracted from that in 2018.

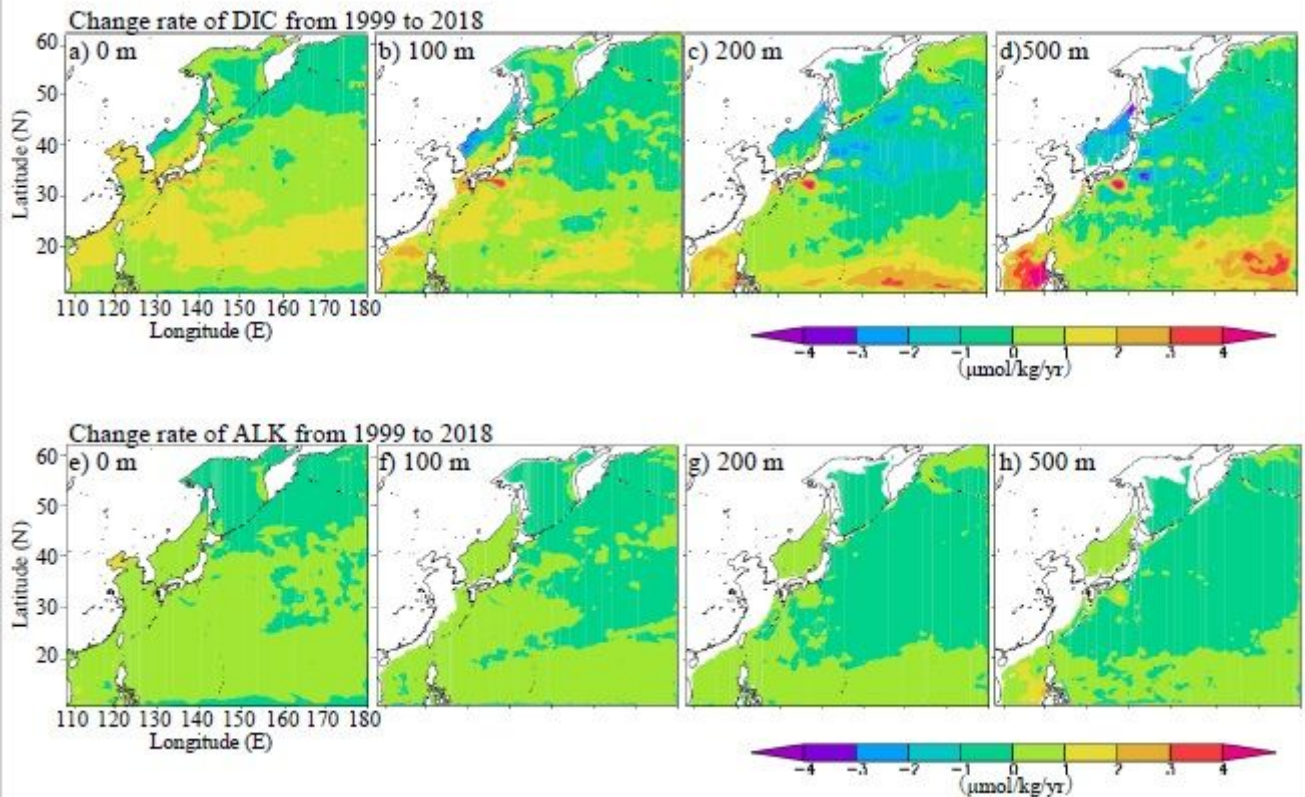


**Figure 4**

Horizontal distributions of change rate of DIC and ALK model outputs from 1999 to 2018 at 0 m, 50 m, 100 m and 200 m depth, respectively. The annual values in 1999 are subtracted from that in 2018.

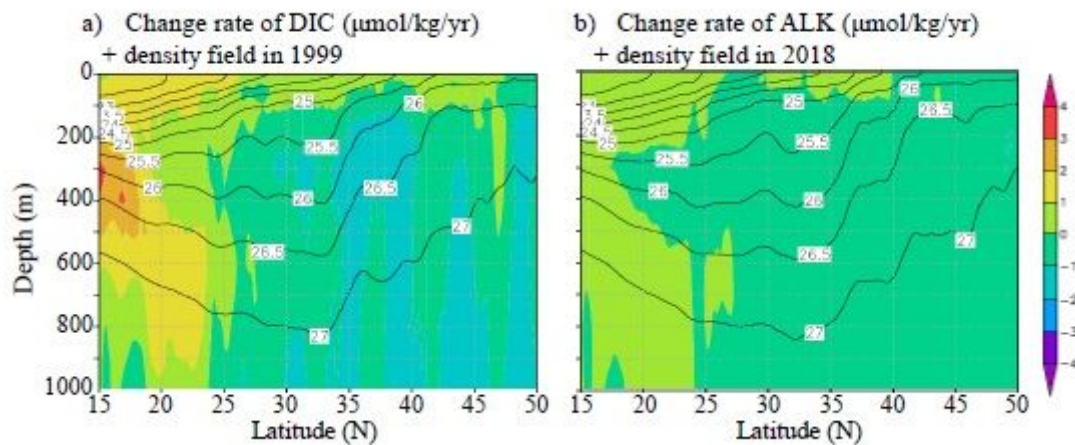


**Figure 5**

Vertical sections of change rate of model outputs for DIC and ALK, respectively, between 1999 and 2018, along the corresponding 165E line. The annual values in 1999 are subtracted from that in 2018. Density contours in a and b are drawn for 1999 and 2018, respectively.

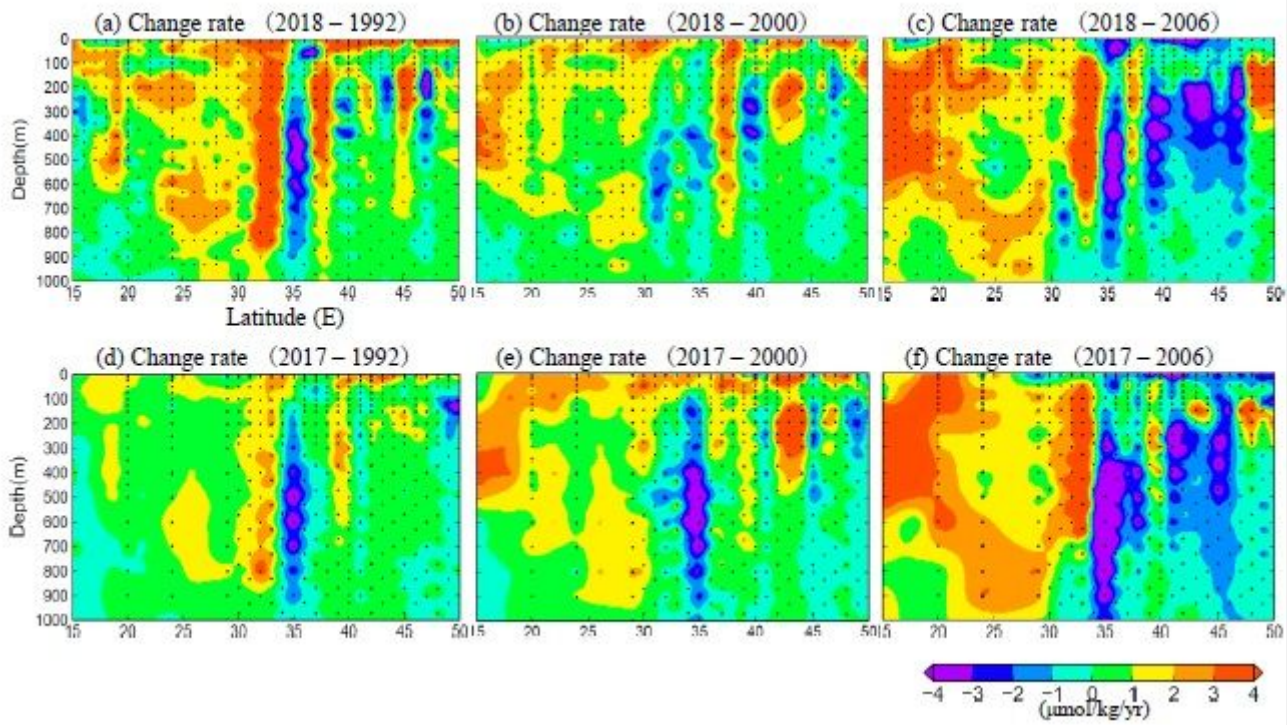


**Figure 6**

Vertical sections of change rate of observed DIC from 2018 (a-c) and 2017 (d-f) to 1992, 2000, 2006, 2011 respectively, along 165°E line.

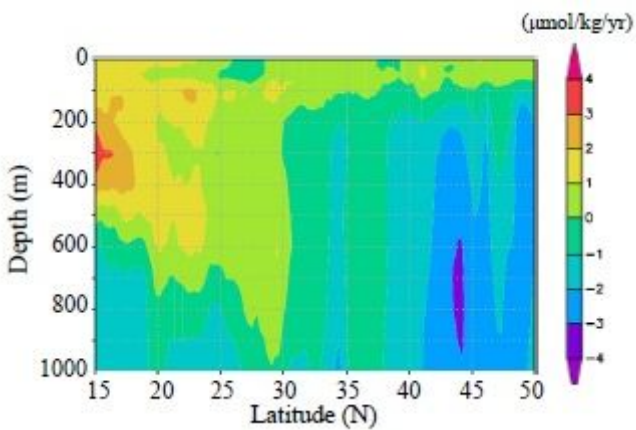


**Figure 7**

Same as Fig. 5a, but between 1995 and 2018.

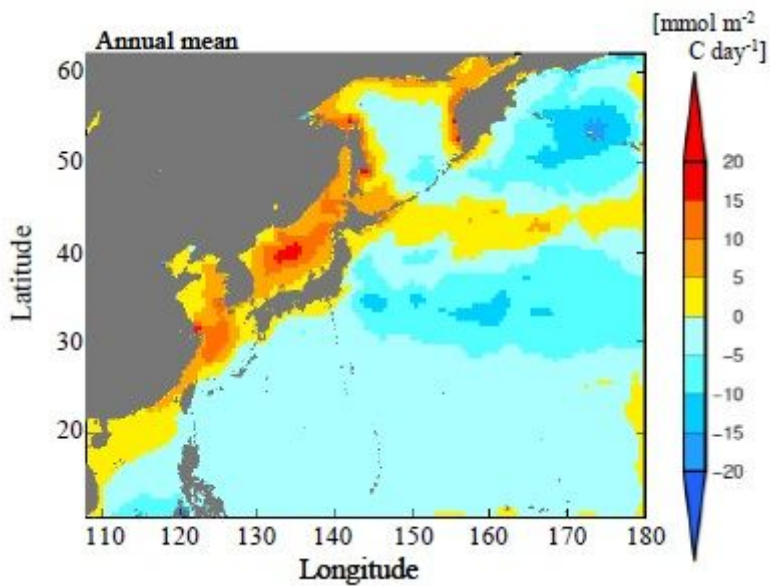


**Figure 8**

Annual mean of air-sea CO<sub>2</sub> flux from 1999 to 2018. Positive and negative values indicate CO<sub>2</sub> uptake and CO<sub>2</sub> release, respectively.

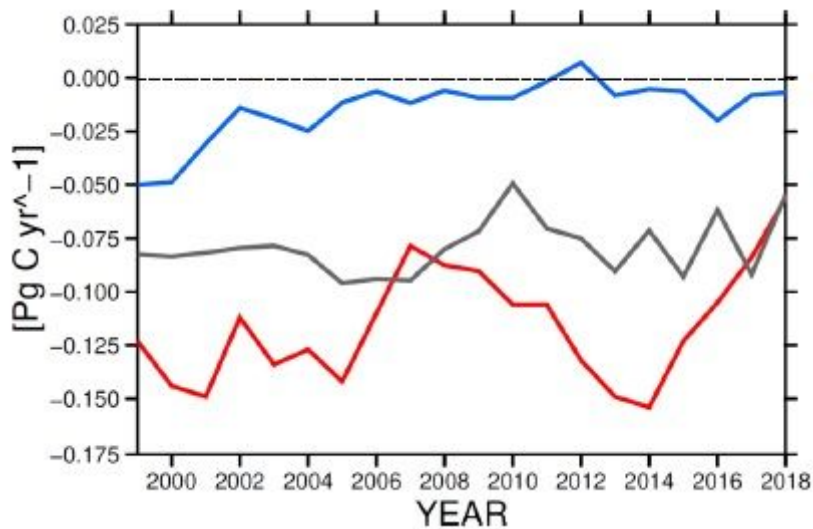


**Figure 9**

Time-series of annual air-sea CO<sub>2</sub> fluxes from 1999 to 2018 in the subarctic region (blue), the Kuroshio extension (red), and the subtropical region (gray), respectively. The annual air-sea CO<sub>2</sub> flux is divided in the subarctic region within (155°–175°E, 40°–50°N), the Kuroshio extension within (142°–175°E, 30°–40°N), and the subtropical region within (130°–175°E, 15°–30°N), respectively. Positive and negative values indicate CO<sub>2</sub> uptake and CO<sub>2</sub> release, respectively.

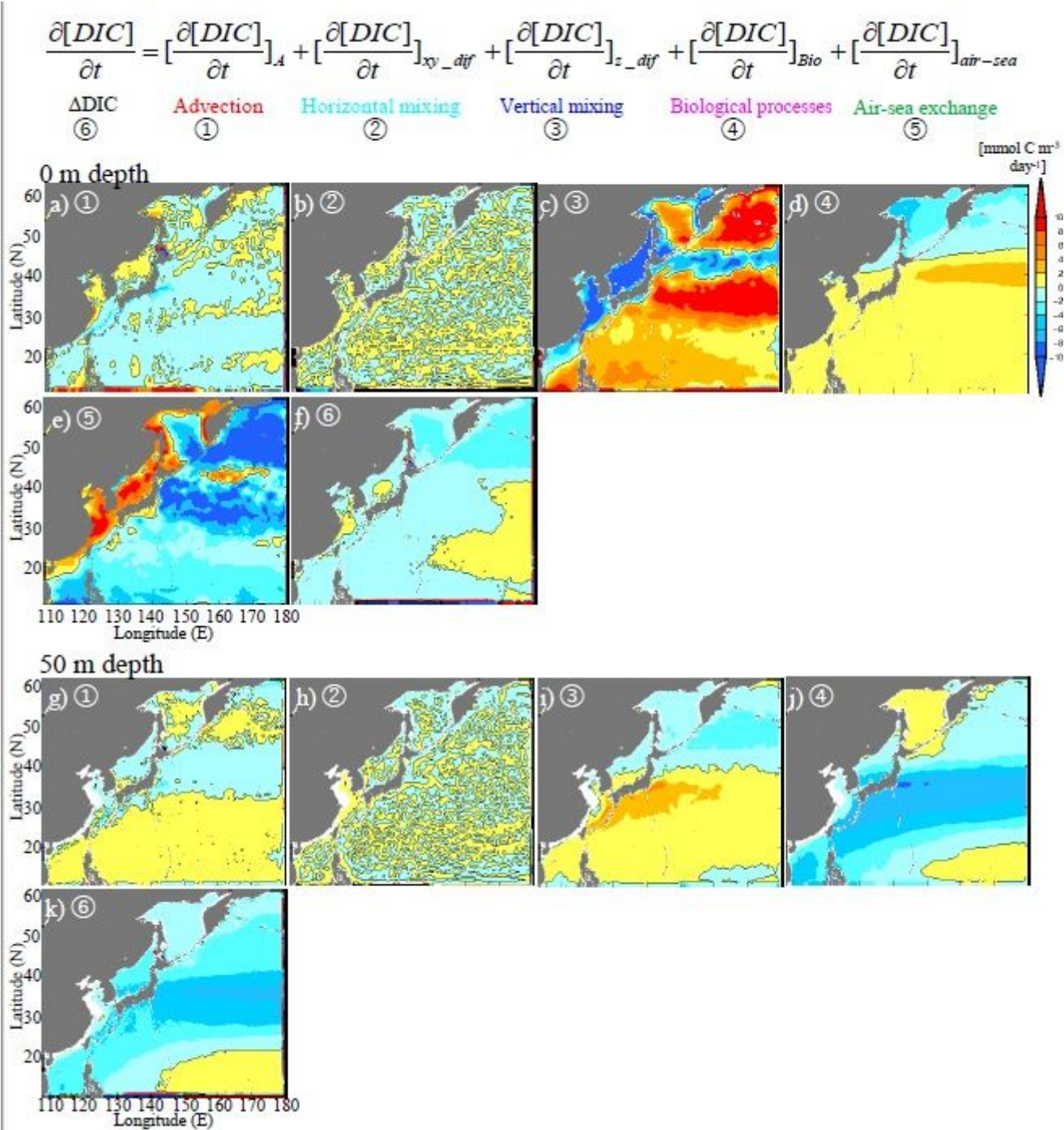


**Figure 10**

Horizontal distributions of yearly DIC variation terms generated by advection (a, g), horizontal diffusion (b, h), vertical mixing (c, i), biological processes (e, j) and air-sea CO<sub>2</sub> exchange process (e) and total DIC time variation (f, k) at 0 m (a-f) and 50 m (g-k) depth, respectively, on the equation above. Positive and negative values indicate increase and decrease in each term for their DIC variations, respectively. The DIC variation term influenced by the air-sea CO<sub>2</sub> exchange are considered only in the surface, not below it.

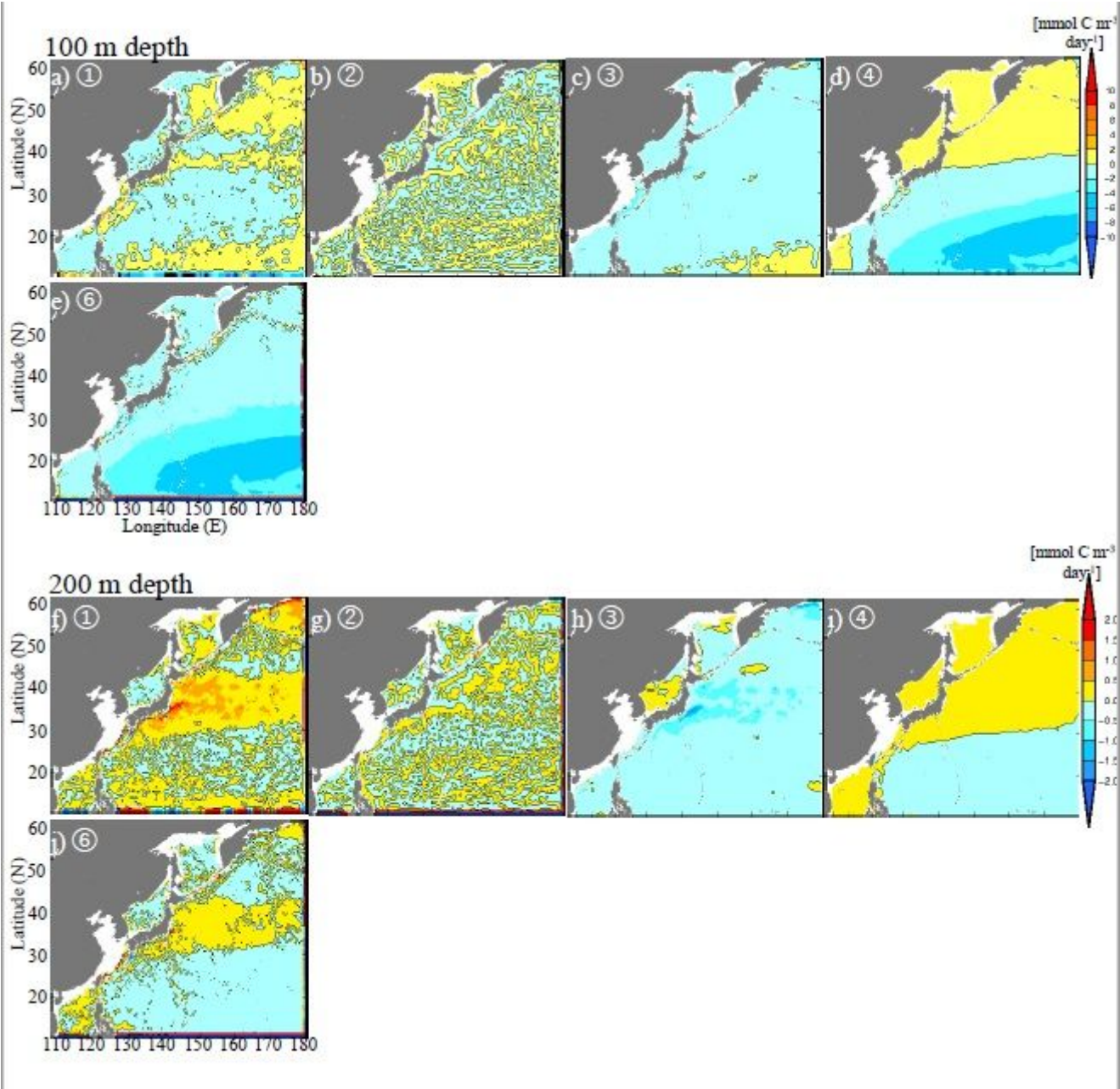


**Figure 11**

Same as Fig. 10, but horizontal distributions of yearly DIC variation terms generated by advection (a, e), horizontal diffusion (b, f), vertical mixing (c, g), biological processes (e, h) and total DIC time variation (d, i) at 100 m (a-d) and 200 m (e-i) depth, respectively.

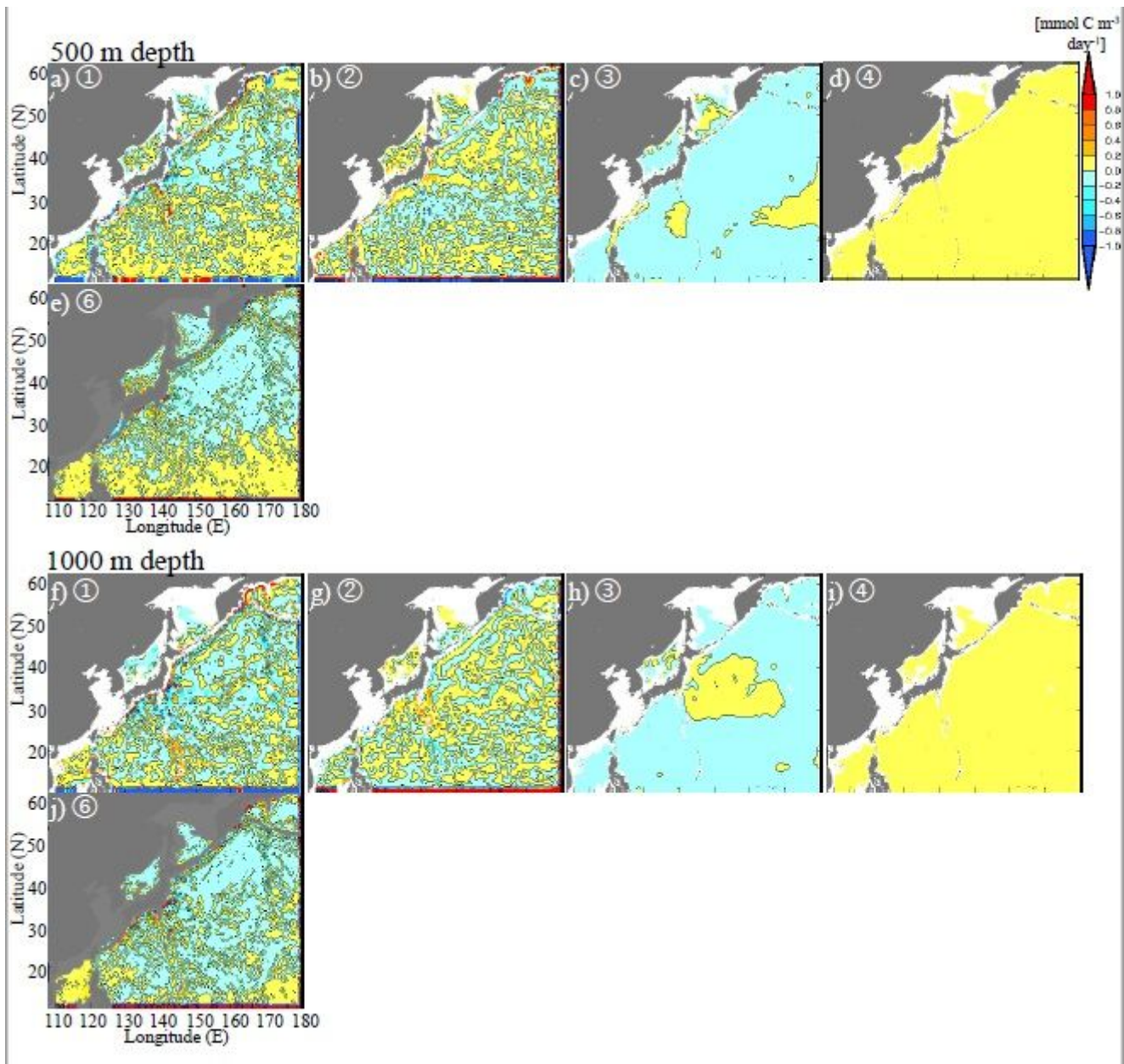


**Figure 12**

Same as Fig. 10, but horizontal distributions of yearly DIC variation terms generated by advection (a, e), horizontal diffusion (b, f), vertical mixing (c, g), biological processes (e, h) and total DIC time variation (d, i) at 500 m (a-d) and 1000 m (e-i) depth, respectively.

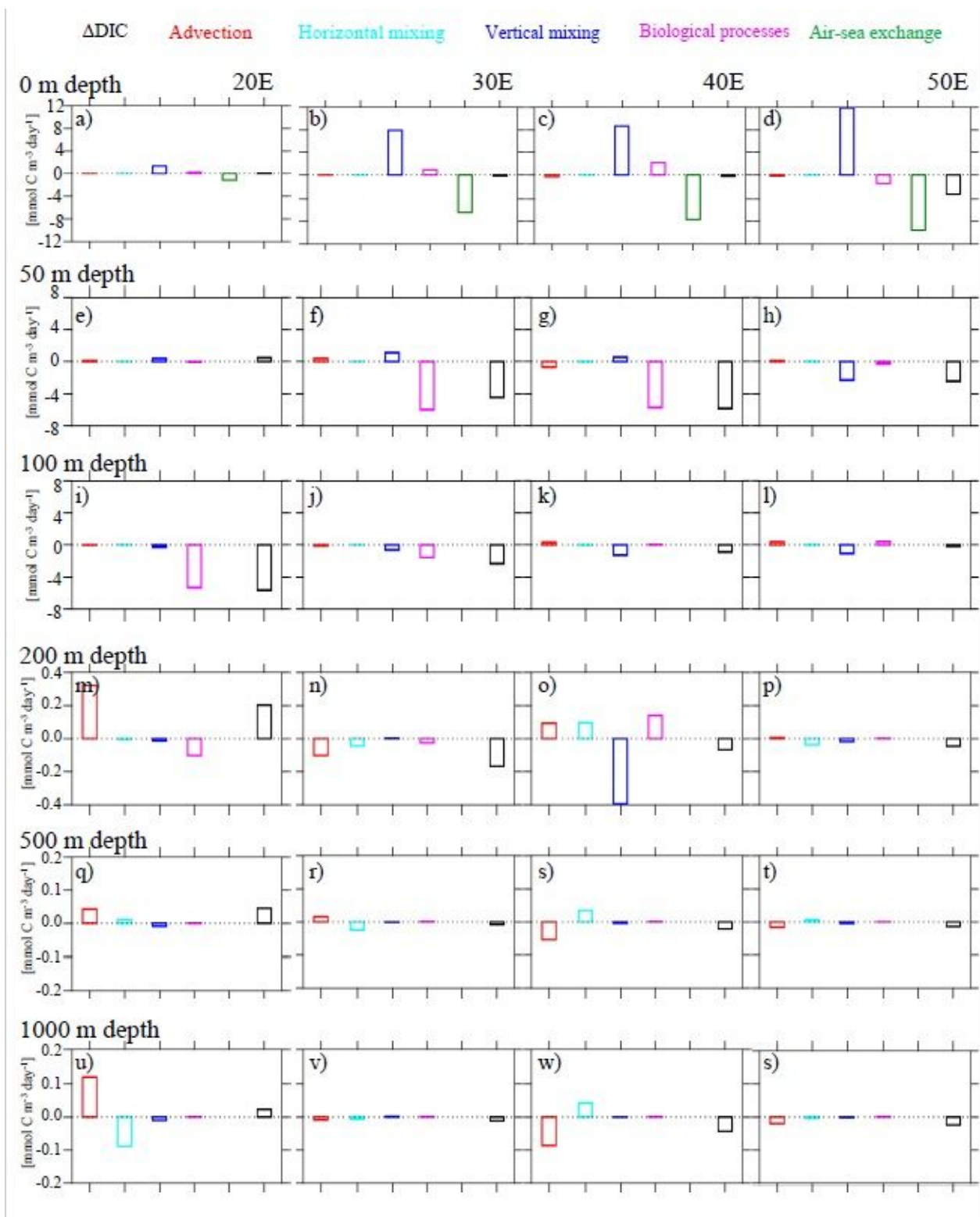


**Figure 13**

Bar graphs of yearly DIC variation terms generated by advection, horizontal diffusion, vertical mixing, biological processes and air-sea CO<sub>2</sub> exchange process and total DIC time variation at 0 m (a-d), 50 m (e-h), 100 m (i-l), 200 m (m-p), 500 m (q-t), and 1000 m (u-s) depth, respectively, at the locations of 20°E (a, e, i, m, q, u), 30°E (b, f, j, n, r, v), 40°E (c, g, k, o, s, w) and 50°E (d, h, l, t, s) along the corresponding 165°E line.

The yearly mean values calculated within the range of 5-grid (22-45.5 km) from the target region. Color bars indicate the same color showing influencing processes in Fig. 10.

## Supplementary Files

This is a list of supplementary files associated with this preprint. Click to download.

- [FigureA.pdf](#)
- [Table1.pdf](#)